Micrometric deformation imaging at W-Band with GBSAR

Arturo Martínez*, Albert Aguasca, Marc Lort and Antoni Broquetas

Department Signal Theory and Communications, Universitat Politècnica de Catalunya,
C/ Jordi Girona 1-3, 08034, Barcelona, Spain
*Corresponding author, e-mail address:arturo.martínez.cervera@gmail.com

Abstract

The paper presents the experimental evaluation of 94 GHz CW-FM Radar that can be configured as a Ground Based SAR (Synthetic Aperture Radar) for high resolution imaging and deformation control. This system has been designed to obtain and analyze data of deformations on different types of bodies, being able to detect range changes of the order of micrometers. After indoor testing and validation measurements, several experimental results obtained in different scenarios are presented. Finally the possibility of using the system for remote contact-less patient monitoring is analyzed.

Keywords: W-Band radar, Ground Based Synthetic Aperture Radar, deformation and vibration control, vital parameters monitoring.

Introduction

Several Ground Based Synthetic Aperture Radars (GBSAR) have been developed in the recent years [Aguasca et al., 2004], [Nico et al., 2004], [Pipia et al., 2006], most operating in the range between 5 to 20 GHz. GBSAR has been proposed to control terrain and infrastructures stability and deformations [Casagli et al., 2010; Luzi et al., 2012; Iglesias et al., 2014; Pratesi et al., 2015]. Continuous Wave Frequency Modulation (CW-FM) configurations have been chosen in most systems, achieving the required illumination energy with low transmitted power. An alternative potential application of low-power radars which has been considered in this work is vital sign detection and monitoring based on induced Doppler shift [Li and Lin, 2008]. The present availability of moderate cost components at millimeter-wave Bands allows to investigate the operation of these systems at W-Band [Abril et al., 2011] and above [Mencia-Oliva et al., 2013], resulting in enhanced spatial resolution and deformation sensitivity compared to usual lower GBSAR frequencies such as Ku-Band. In this paper a 94 GHz GBSAR with a 1.5GHz bandwidth is used to obtain high resolution images and interferometric deformation measurements. After the system description, the test and validation is presented based on experimental trials in anechoic chamber and outdoors. Lastly, the potential uses of the system in infrastructure stability control and vital parameters monitoring have been assessed by experimental data acquisition campaigns and subsequent processing and analysis.

System Description

The system main parts are a CW-FM radar developed in our laboratory operating at 94 GHz (Fig. 1) and a linear positioner unit used to control the radar movement along the synthetic aperture (Fig. 2). The echo signal acquisition subsystem is a commercial digitizer based on the PXI PC-based modular instrumentation standard, complemented with a Direct Digital Synthesizer (DDS) and microwave up-converter to generate a highly linear FM waveform. To ensure stable coherent radar operation, the system local oscillators, DDS and digitizer clocks are synchronized to the system Master Clock, a temperature stabilized crystal oscillator. To simplify the echo processing, a fundamental mixer obtains a de-ramped low frequency beating tone, which is the difference between instantaneous transmitted and received frequencies [Aguasca et al., 2004].
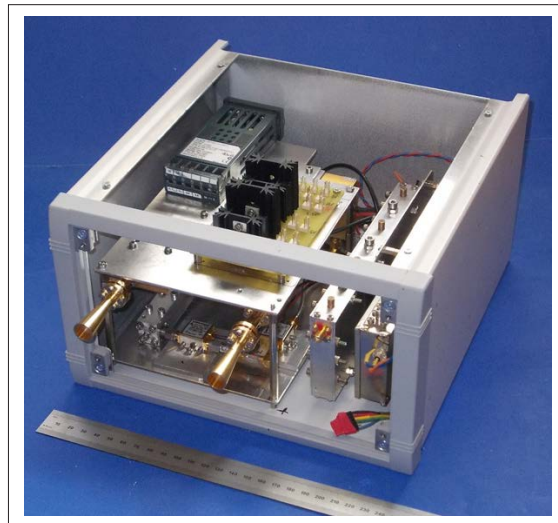

Figure 1 - W-Band Radar used in the system.

Figure 2 - Radar mounted on the linear positioner.

The obtained signal is digitized and processed with a personal computer to obtain range-compressed range profiles and SAR images. The radar is composed of four main modules shown in Figure 3, using horn antennas with 15 dB gain and 13º beamwidth in both transmitter and receiver. The radar can be configured to operate in synthetic aperture mode using a linear positioner, which can be operated in two modes, "Stop & Go" and "On the Fly" as illustrated in Figure 4. In the first case the linear positioner moves the radar at fixed pre-established positions, regularly spaced to take static measurements. This approach offers ideal SAR geometric repeatability between acquisitions with a typical step of 1 to 2 mm and an acquisition time from 3 to 6 minutes. In the "On the Fly" mode the radar acquires the echo signals without stopping, reducing the acquisition time to less than 17 seconds. In the "On the Fly" fast acquisition mode, an optoelectronic acquisition trigger synchronism has been installed in the linear positioner to achieve SAR repeatability between measurements. The linear unit used has a maximum displacement span of 800 mm, a positioning repeatability of ±0.02 mm and a backlash of 0.1 mm or less. Using a sample of the transmitted signal as Local Oscillator in the receiver mixer, the echo range compression is obtained with a Fourier transform [Aguasca et al., 2004]. The azimuth focusing of the range-compressed matrix is achieved with a backpropagation algorithm [Soumekh, 1999], which takes into account the slight bistatic configuration. Table 1 contains the main radar parameters.
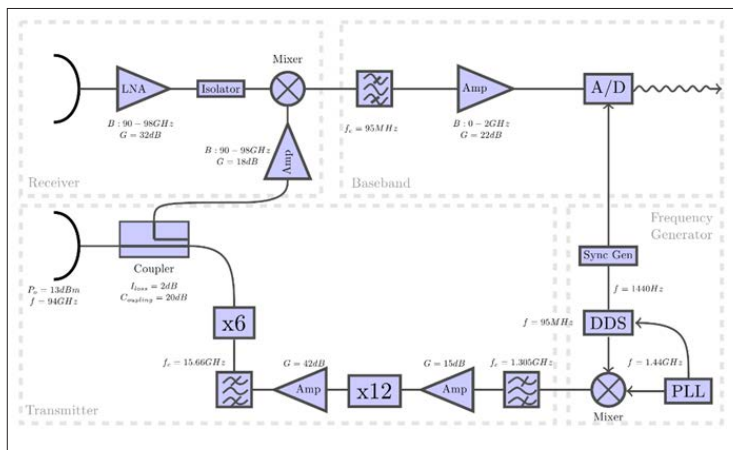

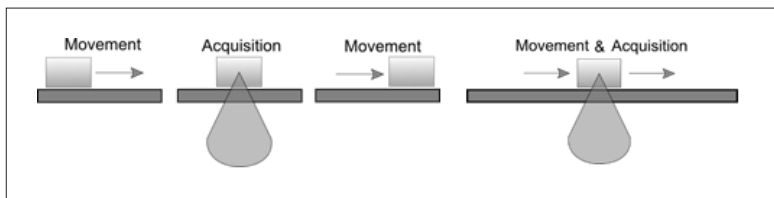**Figure 3 - Radar block diagram.**

Figure 4 - Stop & Go mode (left) and On The Fly (right) acquisition modes.

<div align="center">**Table 1 - Main Radar system parameters.**</div>

Carrier Frequency	f_0 = 94 GHz
Transmitted Power	Pt = 13 dBm
FM sweep repetition freq.	SRF = 1.3732 kHz
Chirp transmitted bandwidth B	B = 1.512 GHz
Antenna Gain	Ga = 15 dB
Noise factor	F = 5.08 dB
Linear positioner span	L_p = 0.7 m
Range resolution	ΔR = 10 cm
Azimuth resolution	Δx = 7.03 mm when R ≤ R_c
Azimuth resolution (farther than critical distance)	Δx = 2.28 mm · R when R > R_c
Critical distance	R_c = 3.08 m

The system has a theoretical range resolution ΔR determined by the FM sweep bandwidth B which has been experimentally confirmed using point targets such as metallic trihedrals.

$$\Delta R = \frac{c}{2B} = 10 \; cm \quad [1]$$

The cross-range resolution is constant for very short ranges where the synthetic aperture length is limited by the antenna beamwidth, which is the usual case in air-borne or space-borne stripmap SAR.

$$\Delta x = \frac{\lambda}{2\theta_H} = 7.03 \; mm \; \left(R \leq R_c \; beam \; limited \; SA \right) \quad [2]$$

However, in GBSAR when the range increases the synthetic aperture is limited by the positioner length resulting in a range dependent cross-range or azimuth resolution.

$$\Delta x = R\frac{\lambda}{2L_p} = R \cdot 2.28 \; mm \; \left(R > R_c \; positioner \; limited \; SA \right) \quad [3]$$

The border between the two regions is the critical Range which in our case is $R_c = 3.08 \; m$. The radar has a maximum range operating distance of 203 m and a minimum operating distance of 40 cm. The minimum detectable target Radar Cross Section is range dependent as depicted in Figure 5.
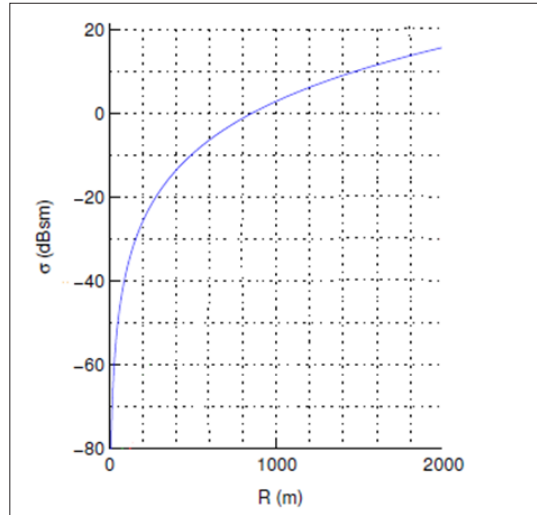
Figure 5 - Detectable Radar Cross Section with respect to target range.

System testing and validation

To validate the system, the first step was to assure the correct detection of the targets checking their SAR imaged position was coincident with the scene true geometry. In addition, the phase stability of the system over time was evaluated experimentally, since this parameter will determine the precision in the intended micrometric motion detection.

Geometric accuracy validation

The geometric accuracy was validated using three canonical targets (a metallic cylinder and two trihedrals) deployed in controlled positions in anechoic chamber, as shown in Figure 6. To carry out the geometric accuracy validation of the system, the scenario was measured four times in each of the acquisition modes, "Stop & Go" and "On the Fly", obtaining the same image for all the measurements, which is shown in Figure 7. In the "Stop & Go" acquisition, multiple measurements are usually carried out in each radar position, for example 100 measurements/position do not introduce significant measurement delay and provide a 20 dB Signal-to-Noise Ratio (SNR) increase compared to a single acquisition per position baseline. Although no explicit averaging is carried out in the "On the Fly" mode, the inherent azimuth oversampling of the radar Sweep Repetition Rate results in more than 20.000 samples contributing to the Synthetic Aperture that after SAR processing results in 15 dB SNR increase with respect single acquisition per position Stop & Go reference bseline. In summary, comparing both acquisition modalities, "Stop & Go" provides slighltly better SNR at the price of a slower acquisition whereas On the Fly allows a faster acquisition with slightly worse SNR. The table of Figure 7 shows the true location of the targets A, B and C in X, Y coordinates being the first radar location in the linear positioner the origin of coordinates. The labelled positions in the Figure 7 image, which has been obtained in the Stop & Go mode, show that the targets appear at the expected positions with an error below 1.5 cm.
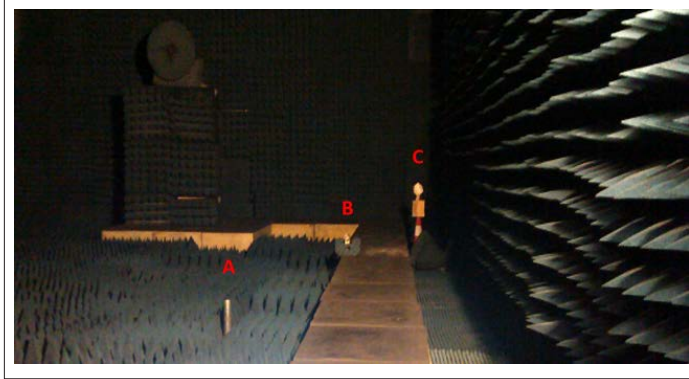
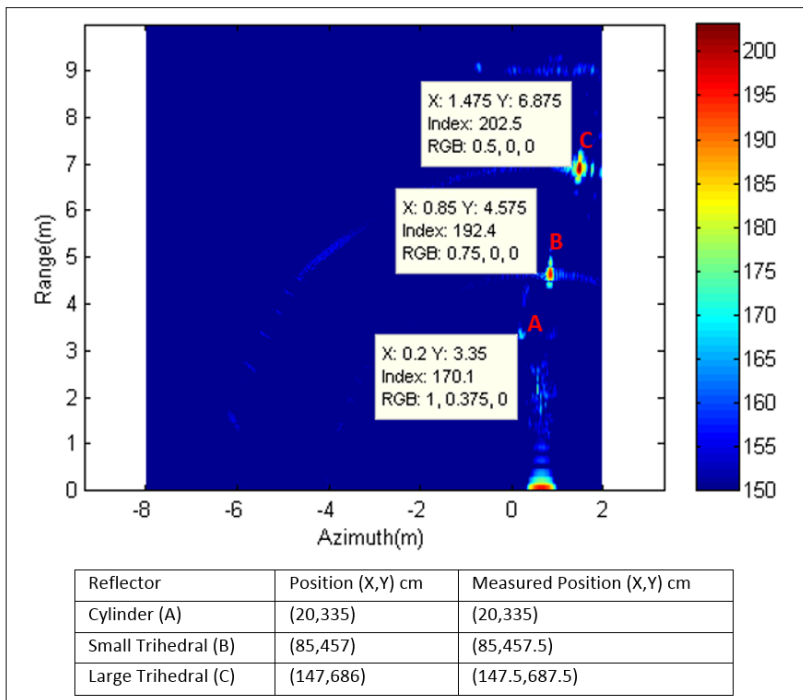**Figure 6 - Geometric accuracy and deformation validation scenario.**

Reflector	Position (X,Y) cm	Measured Position (X,Y) cm
Cylinder (A)	(20,335)	(20,335)
Small Trihedral (B)	(85,457)	(85,457.5)
Large Trihedral (C)	(147,686)	(147.5,687.5)

Figure 7 - Image of validation scene with geometric accuracy validation results.

System stability

The stability of the system was one of the priorities of the research, due to the strong phase change that a thermal drift could cause at 94 GHz. A series of measurements were acquired in a small 3 x 3 m² anechoic chamber every 30 minutes during one day to determine the long-term radar phase stability. Three stable metallic reflectors: 2 trihedrals and a cylinder were placed at increasing distances in a small anechoic chamber in front of the radar. The phase variation obtained is shown in Figure 8. The first 5 measurements show a positive phase

slope, essentially the same for the three targets which corresponds to the system warming-up, since the system was cold-started without previous thermal control. When the system achieves thermal stabilization, a negative phase-drift is observed which is proportional to the target range. Since the anechoic chamber was closed during the experiment with the radar and the PXI based digitizer dissipating around 200 W of power inside, this phase change might have been caused by internal chamber air heating resulting in air index of refraction change.

The thermal stabilization of the radar uses heating resistors and a ventilator that are activated by a proportional-integral-derivative controller which keeps the radar at 35°C +/- 0.5°C. The peak to peak phase ripple around 0.025 radians, is assumed to be caused by the internal temperature fluctuations, which using the radar wavenumber translates into an intrinsic 6.35 μm uncertainty excluding atmospheric propagation changes.
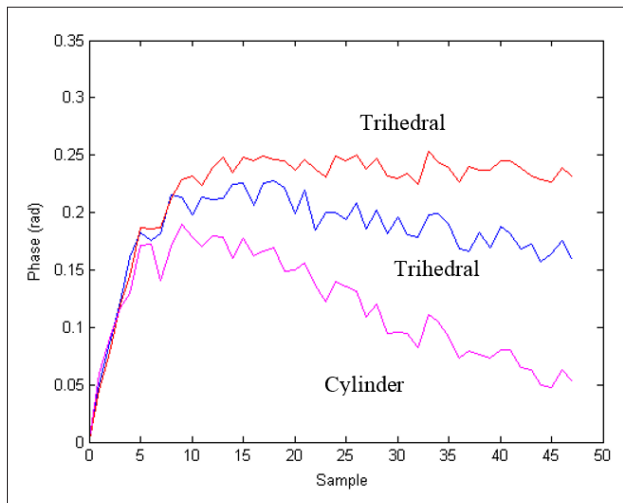

Figure 8 - Phase variation over 24 hours observed in anechoic chamber for a near-range trihedral located at R=0.8 m from the radar (red line), a medium range trihedral located at R=1.5 m from the radar (blue line) and a far range cylinder located at R=2.5 m from the radar (purple line).

To assess the effect of atmospheric changes on the measurements, a second experiment was carried out outdoors. In this case the synthetic aperture radar acquisitions were taken every 5 minutes from 7:30 to 9:30 H and three nearby sensors measuring temperature, pressure and humidity were used to control the atmospheric changes. In the elapsed time of the experiment the air temperature increased and air moisture decreased due to sunlight heating and ground dew evaporation. Figure 9A shows the measured phase change evolution of three trihedrals located at 16.2 m, 27.7 m and 37.5 m from the radar. Figure 9B shows the phase change predicted by a model using the temperature/pressure/humidity nearby measurements. The agreement between phase change measured and predicted is not perfect since the radar integrates the atmospheric propagation changes along the signal path whereas the measurements were taken at a single point located around 3 m from the

center of the radar signal path. However, the predicted phase trend is correct which shows the importance of appropriate atmosphere modeling to obtain deformation measurements in case of changing meteorological conditions.

To predict the air permittivity change a UIT-recommended model [ITU, 1999] was used where the air refractivity index N is defined by Equation [4], magnifying the index of refraction n changes by a factor 10^6.

$$N = (n-1) \cdot 10^6 \quad [4]$$
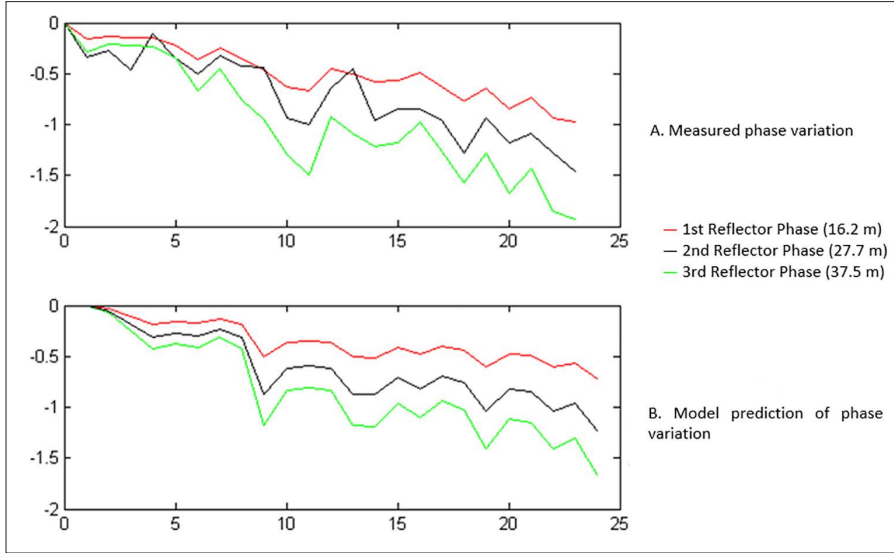
Figure 9 - Phase change comparison in outdoor three trihedrals SAR observation every 5 minutes during 2 hours. A: Measured phase variation. B: Predicted phase variation from air temperature, pressure and humidity parameters measurements near the radar signal path.

The resulting phase change $\Delta\varphi ATM$ induced by atmospheric changes is expressed in Equation [5], where f_c is the radar carrier frequency, r_n is the range of the observed target and c the speed of light in vacuum

$$\Delta\varphi ATM = 10^{-6} \cdot \frac{4\pi f_c r_n}{c} \cdot \Delta N \quad [5]$$

The refractivity index N can be decomposed in the dry and wet components as expressed in Equations [6] and [7]

$$N_{dry} = \frac{77.6 \cdot p}{T} \quad [6]$$

Where p is the atmospheric pressure (hPa) and T the absolute temperature in Kelvin

$$N_{wet} = \frac{3.73 \cdot 10^5 \cdot w_p}{T^2} \quad [7]$$

Where w_p is the water vapor pressure (hPa) which can be obtained from the knowledge of the relative humidity H % and temperature.

$$w_p \cong 6.11 \cdot e^{\left(19.7 \cdot \frac{T-273}{T}\right)} \cdot H \quad [8]$$

This model can be used up to 100 GHz with an error under 0.5%.

Micrometric change detection
The validation of small motion detection was carried out using the set-up of the first experiment shown in Figure 6. The small trihedral reflector B was moved with a micrometric positioner. Measurements with line of sight displacements of the trihedral ranging from 60 μm to 1.04 mm were carried out in the "Stop & Go" mode. The displacement shown in the center of Figure 10 corresponds to the smallest range change of 60 μm. The metallic cylinder A was imaged with no phase changes as expected. However, the image also shows an unexpected stability problem affecting trihedral C due to the lack of rigidity of the used rubber traffic-type conic support. After system validation, different experimental campaigns were made to ascertain the potential of the radar in different fields.
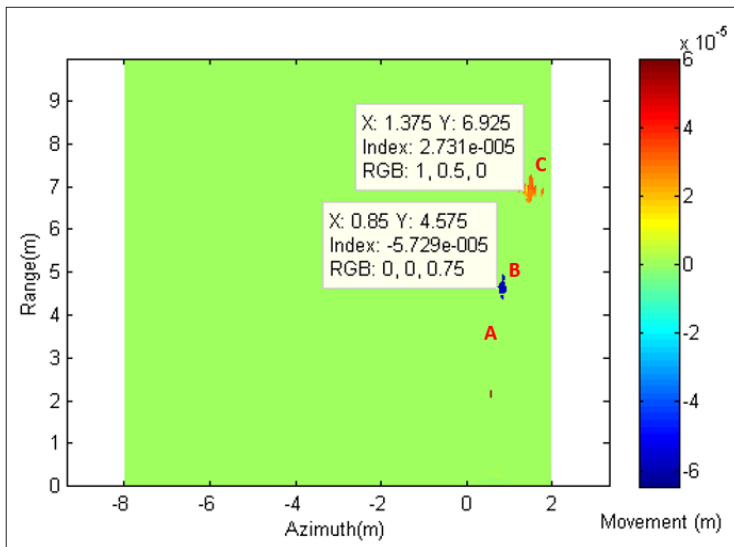
Figure 10 - Micrometric motion detection. Index value shows the detected motion in meters of targets B and C.

Experimental evaluation of infrastructure control

To test the capability of the system in real infrastructure deformation control, an interferometric change observation of a railway bridge during train passages has been carried out. The radar was operated underneath the bridge, near one of the support columns and looking to the center of the segment between two consecutive support columns, as shown in Figure 11, where the radar position has been circled in red. In this case, the radar was configured as a real-aperture ranging instrument able to measure target amplitude, range and phase.

Figure 11 - Railway bridge measurement scenario. The red circle indicates the radar location.

After taking several reference measurements, acquisitions were made during the passage of the train over the railway segment at the FM Sweep Repetition Frequency SRF = 1.3732 kHz. The spatial and time evolution of the bridge deformation of one of the train circulations over the bridge can be observed in Figure 12.
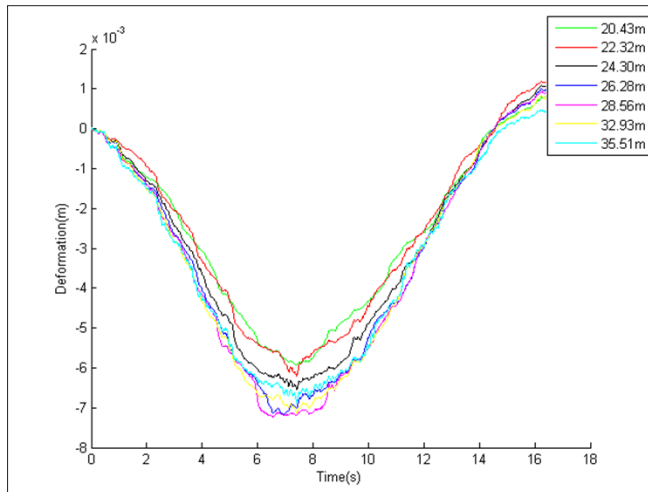
Figure 12 - Railway bridge deformation results.

The phase evolution of a selection of bridge bright scattering points has been tracked and expressed in radial deformation in the radar direction in meters. It is possible to observe

that the center part is the one that suffers the most pronounced deformation, with a peak of 7 mm in the radar direction. A slight bridge uplift can be observed beyond t = 14 s which is caused by the leveraging of the train-head located beyond the column delimiting the observed track. In Figure 12, it is also possible to observe the vibrations caused by the train circulation through the bridge. A detail of the train-induced vibration is shown in Figure 13, it is worth noting that the vertical scale ticks correspond to 100 μm displacement in the radar direction, the signal is very clean showing details of the motion in the order of 10 μm resolution.
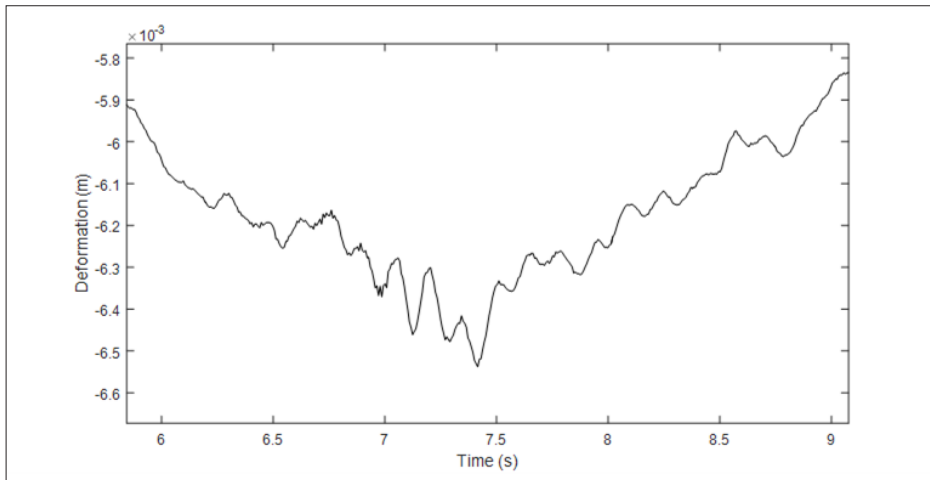

**Figure 13 - Detail of bridge vibration measured in bridge point located at 24.3 m from radar.**

Experimental assessment of biomedical applications

Lastly, the possibility of using the system to control the vital parameters of a patient without physical contact was assessed using this system. A student simulated a patient in the laboratory laying horizontally on a bed underneath the radar with the antennas pointing down to his chest. Different situations were simulated: a relaxed patient with normal respiration, patient suffering a seizure, restless sleeping and apnea. After processing the measurements the plots shown in Figure 14, 15 and 16 were obtained. In Figure 14 the blue line presents the phase-change retrieved motion of a relaxed patient laying still on bed breathing normally, the red line shows the data obtained measuring the patient trembling simulating a seizure. In the first case, the breathing pattern is easily identified, some smaller blood pulse induced transients can be seen superimposed on the main breathing component. In the seizure simulation case, the signal pattern is completely different and easily detectable containing information on the amplitude and spectrum of the abnormal motion. Figure 15 shows the radial distance waveform corresponding to a simulated restless sleep, introducing irregularities on the breathing pattern of a relaxed sleep. Figure 16 shows the student chest motion obtained by the radar in apnea condition after having done physical exercise. In this case a blood pulse waveform is clearly observed. A zoom of one of the obtained pulses is shown in Figure 17 which compares very well with the typical arterial pulse waveform of a healthy person, showing details that have diagnostic relevance about the circulatory system
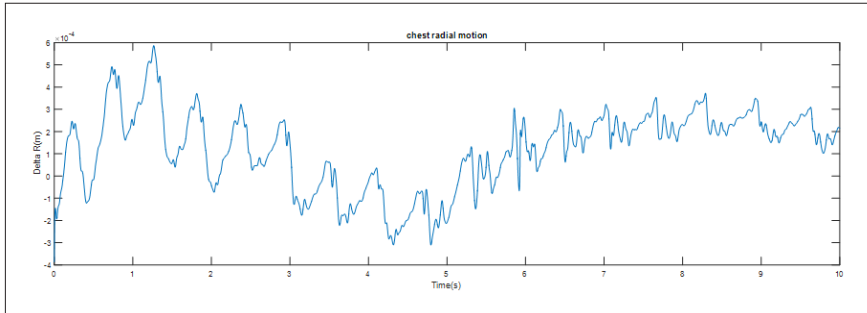
condition [Stoner et al., 2012]. It is worth noting the clean waveform obtained in Figure 17, considering the tick distance of the vertical axis (50 µm) which evidences the micrometric motion detection capability of this technology.
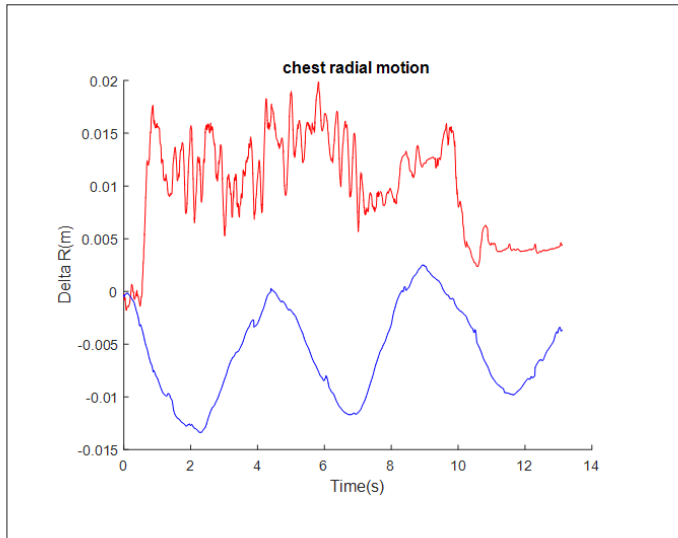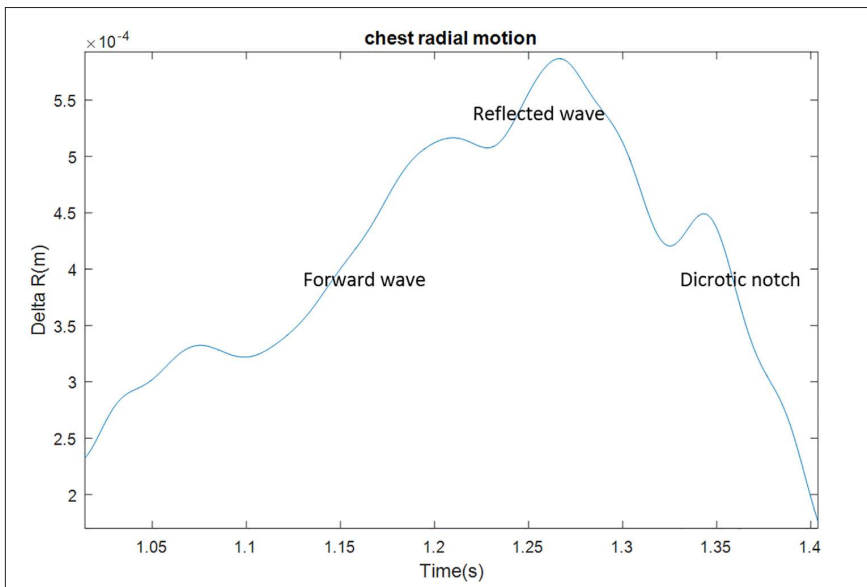

Figure 14 - Normal breathing motion measurement (blue) and seizure simulation (red).
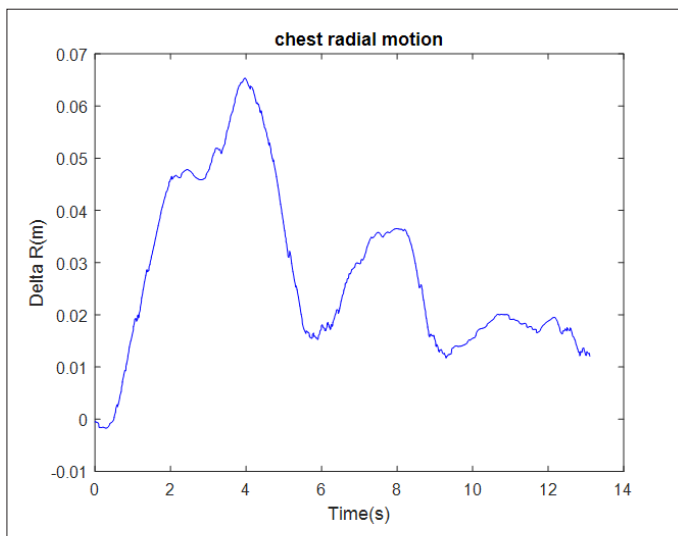
Figure 15 - Unrest motion during sleep (simulation).

Figure 16 - Pulse detection without breathing.

Figure 17 - Single Blood Pulse waveform showing typical pulse pattern and characteristic features.

Conclusions

CW-FM Ground Based radars working at 94 GHz can be used to form SAR images of nearby scenes with high resolution exploiting a larger transmitted bandwidth and electrically larger synthetic apertures compared to conventional GB-SAR. Processing the image phase changes, very small target deformations in the order of few micrometers can be detected thanks to the large radar wavenumber at W-Band. The high phase sensitivity with respect to echo delay results also in a very noticeable impact of air refraction changes on the observed phase. With fast data acquisition, atmospheric changes may have a neglectable impact on the detected deformation, otherwise the observations should be carried out in periods of low atmospheric change, or compensate the air refractivity changes using a model fed by in-situ measurements of temperature, pressure and humidity. After laboratory testing and

validation, the radar has been able to remotely measure micrometric structural deformation and vibration of a bridge in the observation direction. Additional synchronized radar observations could be carried out in different angles to determine the 3D components of the observed motion. Preliminary assessment of W-Band radars biomedical application, has revealed the capability of contact-less monitoring of vital constants. Results indicate that abnormal patient conditions affecting body motion could be characterized and detected. Blood pulse signatures have been observed with excellent agreement with arterial pressure waveforms and will be further investigated to assess the applicability of radar technology for contact-less diagnostics.

Acknowledgements

References
Abril J., Nova E., Broquetas A., Aguasca A., Romeu J., Jofre L. (2011) - *Micrometric deformation imaging at W-Band*. Proceedings of the 2011 IEEE International Microwave Workshop. IMWS, pp. 65-68. doi: http://dx.doi.org/10.1109/imws3.2011.6061889.

Aguasca A., Broquetas A., Mallorqui J.J., Fabregas X. (2004) - A *Solid State L to X-band Flexible Ground- Based SAR System for Continuous Monitoring Applications*. Proceedings of the IEEE International Geoscience and Remote Sensing Symposium, IGARSS 2004, Anchorage, AK, USA, September 2004, pp. 757-760. doi: http://dx.doi.org/10.1109/IGARSS.2004.1368512.

Casagli N., Catani F., Del Ventisette C., Luzi G. (2010) - *Monitoring, prediction, and early warning using ground-based radar interferometry*. Landslides, 7 (3): 291-301. doi: http://dx.doi.org/10.1007/s10346-010-0215-y.

Iglesias R., Fabregas X., Aguasca A., Mallorqui J.J., López-Martínez C., Gili J.A., Corominas J. (2014) - *Atmospheric phase screen compensation in ground-based SAR with a multiple-regression model over mountainous regions*. IEEE Transactions on Geoscience and Remote Sensing, 52 (5): 2436-2449. doi: http://dx.doi.org/10.1109/TGRS.2013.2261077.

Li C., Lin J. (2008) - *Random Body Movement Cancellation in Doppler Radar Vital Sign Detection*. IEEE Transactions on Microwave Theory and Techniques, 56 (12): 3143-3152. doi: http://dx.doi.org/10.1109/TMTT.2008.2007139.

Luzi G., Monserrat O., Crosetto M. (2012) - *The potential of coherent radar to support the monitoring of the health state of buildings*. Research in Non-destructive Evaluation, 23: 125-145. doi: http://dx.doi.org/10.1080/09349847.2012.660241.

Mencia-Oliva B., Grajal J., Yeste-Ojeda O.A., Rubio-Cidre G., Badolato A. (2013) - *Low-Cost CW-LFM Radar Sensor at 100 GHz*. IEEE Transaction on Microwave Theory and Techniques, 61 (2): 986-998. doi: http://dx.doi.org/10.1109/TMTT.2012.2235457.

Nico G., Leva D., Fortuny-Guasch J., Antonello G., Tarchi D. (2005) - *Generation of digital terrain models with a ground-based SAR system*. IEEE Transactions on Geoscience and Remote Sensing, 43 (1): 45-49. doi: http://dx.doi.org/10.1109/TGRS.2004.838354.

Pipia L., Fabregas X., Lopez-Martinez C., Aguasca A., Mallorquí J. (2006) - *Polarimetric Temporal Decorrelation Studies by Means of GBSAR Sensor Data*. IEEE International Symposium on Geoscience and Remote Sensing, pp. 79-82. doi: http://dx.doi.org/10.1109/IGARSS.2006.25.

Pratesi F., Nolesini T., Bianchini S., Leva D., Lombardi L., Fanti R., Casagli N.(2015) - *Early Warning GBInSAR-Based Method for Monitoring Volterra (Tuscany, Italy) City Walls*. IEEE Journal of Selected Topics in Applied Earth Observations and Remote Sensing, 8 (4): 1753-1762. doi: http://dx.doi.org/10.1109/JSTARS.2015.2402290.

Soumekh M. (1999) - *Synthetic Aperture Radar Signal Processing with MATLAB Algorithms*. John Wiley & Sons; 3rd Edition.

ITU (1999) - *Recommendation Rec. ITU-R P.453-7*. Available online at: https://www.itu.int/dms_pubrec/itu-r/rec/p/R-REC-P.453-7-199910-S!!PDF-E.pdf.

Stoner L., Young J.M., Fryer S. (2012) - *Assessments of arterial stiffness and endothelial function using pulse wave analysis*. International Journal of Vascular Medicine, 2012 903107), 9p. doi: http://dx.doi.org/10.1155/2012/903107.